



Optimal kinematics for energy harvesting using favourable wake–foil interactions in tandem oscillating hydrofoils

Eric E. Handy-Cardenas¹ , Yuanhang Zhu^{1,2}  and Kenneth S. Breuer¹ 

¹Center for Fluid Mechanics, School of Engineering, Brown University, Providence, RI 02912, USA

²Department of Mechanical Engineering, University of California, Riverside, CA 92521, USA

Corresponding author: Eric E. Handy-Cardenas, eric_handy-cardenas@brown.edu

(Received 18 November 2024; revised 7 March 2025; accepted 17 April 2025)

The energy-harvesting performance of two oscillating hydrofoil turbines in tandem configuration is experimentally studied at a Re of 20 000 to determine the array's optimal kinematics. By characterising interactions between the leading foil's wake and the trailing foil, the kinematic configuration required to maximise array power extraction is identified. This is done by prescribing leading-foil kinematics that produce specific wake regimes, identified by the maximum effective angle of attack, $\alpha_{T/4}$, parameter. The kinematics of the trailing foil are varied significantly from those of the leading foil, with heave and pitch amplitudes of $0.6c < h_{0,tr} < 1.8c$ and $65^\circ < \theta_{0,tr} < 75^\circ$, and inter-foil phase of $-110^\circ < \psi_{1-2} < 180^\circ$. Configurations with reduced frequencies of 0.11 and 0.12, and foil separations of $4c$ and $6c$ are tested within each wake regime. The power extracted by each foil over an oscillation cycle is measured through force and torque measurements. Wake–foil interactions that improve trailing foil performance are analysed with time-resolved particle image velocimetry. Constructive and destructive wake–foil interactions are compared, showing that trailing-foil performance improves by either avoiding wake vortices or interacting directly with them. By interacting with the primary wake vortex, the latter configuration sees no power loss during the cycle. System power from the two foils is found to be maximised when the leading foil operates at an intermediate $\alpha_{T/4}$ range, and when the trailing foil avoids wake vortices. This optimal array configuration sees both foils operating with different kinematics compared with the optimal kinematics of a single oscillating foil.

Key words: vortex interactions, wakes, vortex dynamics

1. Introduction

As the need for sustainable energy sources continues to rise, more attention has been paid to tidal flow energy due to its high predictability and abundance when compared with other sources like wind and solar (Uihlein & Magagna 2016; Khare & Bhuiyan 2022). Research into hydrokinetic turbine technologies has grown in the past decade (Xiao & Zhu 2014; Young, Lai & Platzer 2014) due to their promise as tidal flow energy extraction devices, as well as for the fluid phenomena that govern their behaviour. The main types of tidal energy-harvesting turbines are horizontal axis rotary turbines (HATs), vertical axis rotary turbines (VATs) and oscillating foil turbines (OFTs). Both HATs and VATs have some significant disadvantages such as high rotational speeds that can affect local wildlife and a tendency to biofoul. In addition, HATs create messy wakes that interfere with downstream turbines, a crucial issue for efficient array deployments.

First proposed by McKinney & DeLaurier (1981), OFTs extract energy using a wing that moves with a coupled heaving and pitching motion in an oscillating manner with respect to an oncoming flow. The motion can be prescribed (Karakas & Fenercioglu 2016; Kim *et al.* 2017), semi-passive (Su & Breuer 2019; He *et al.* 2022a) or fully passive (Oshkai *et al.* 2022; Zhao *et al.* 2023), depending on how much of the kinematics are directly controlled. The OFT takes advantage of unsteady force generation, where lift, force and pitching moments are generated during the oscillation cycle. The high angle of attack achieved results in the turbines operating within the dynamic stall regime, with flow separation a prominent feature and strong coherent vortices generated during the oscillation cycle. Kinsey & Dumas (2008) and Simpson (2009) identified that highly loaded cases see strong leading-edge vortices (LEVs) formed on the suction side of the foil, resulting in a low-pressure region that induces additional lift on the foil.

Although single-foil performance has been well characterised (Kinsey & Dumas 2008; Kim *et al.* 2017), array configurations are an area of significant research interest (Kinsey & Dumas 2012; Ribeiro *et al.* 2021; Zheng & Bai 2022; Zhao *et al.* 2023). An important characteristic of OFT design is the structured wake that develops behind the hydrofoil. In comparison with a rotary turbine, whose wake is characterised by a cylindrical ‘sheath’ of blade tip vortices (Massouh & Dobrev 2007), the wake behind an OFT develops into an unsteady vortex-dominated flow akin to the von Kármán vortex street (Simpson 2009). This vortex-dominated wake is characterised by a single primary LEV being advected every oscillation stroke that remains coherent several chord lengths downstream. Multiple studies have looked at the wake topology of oscillating foils and, although the focus has been primarily on thrust-producing regimes, similar wake topology characteristics could have important effects for OFT arrays. Notably, Verma & Hemmati (2021) studied the evolution of the wake behind a heaving and pitching foil within a thrust regime and identified a performance setting where the foil operated with high efficiency but low thrust at a low Strouhal number, and which corresponded to cases where wake vortices interacted and coalesced. They observed a second low-efficiency but high-thrust setting that displayed minimal vortex interactions in the wake. In a subsequent oscillating foil study, Verma & Hemmati (2024) characterised the transition of the primary and secondary LEVs to hairpin vortex groups according to an increasing chord-based Strouhal number in propulsive regimes. In a combined numerical and experimental study, Gao *et al.* (2023) looked at the transition and force characteristics of a purely plunging foil at a fixed angle of attack. They noted that the interaction between the LEV and trailing-edge vortex (TEV) was the mechanism responsible for the three-dimensional transition of the wake.

The impact on performance due to the effects of vortex-dominated wakes interacting with downstream turbines is an important consideration for the successful development

of efficient turbine arrays. While a HAT array will have downstream turbines always negatively impacted by interactions with an upstream turbine's wake (Kuang *et al.* 2023), other types of turbines, such as VATs and OFTs, can harness wake–foil interactions to improve array performance. The similar phenomenon of fish schooling and hydrodynamic interactions in swimmer arrays has been studied extensively (Ramanarivo *et al.* 2016; Newbolt, Zhang & Ristroph 2019; Li *et al.* 2020; Wei *et al.* 2023; Gungor, Khalid & Hemmati 2024). Improving array performance by optimising wake–turbine interactions has been studied extensively in VATs. Inspired by the schooling phenomenon, Whittlesey, Liska & Dabiri (2010) proposed a VAT array design using a potential flow model that optimised the turbines' spatial arrangement to increase array performance. Following from this study, Dabiri (2011) studied an array of counter-rotating vertical axis wind turbines (VAWTs) and was able to achieve improved power output per unit area when compared with traditional arrays. This was achieved by optimally arranging VAWTs such that they are able to extract energy from nearby turbine wakes. In a later study, Howland, Lele & Dabiri (2019) tested wake steering in VAWTs to deflect a turbine's wake from downstream turbines and reduce power production variability. Scherl *et al.* (2020) optimised the array geometry, control and turbine rotation direction of a pair of VATs and found that performance increases were achieved due to beneficial mean and periodic flow alterations or blockage.

Harnessing wake–foil interactions to improve an array's energy-harvesting performance depends on properly tuning the turbines' kinematic parameters. In a tandem foil configuration, these parameters are the reduced frequency, f^* , the inter-foil phase, ψ_{1-2} , and the inter-foil distance, S_x (Kinsey & Dumas 2012; Karakas & Fenercioglu 2016; He *et al.* 2022*b*). Tuning these parameters affects the timing of interactions, the magnitude of these effects and ultimately the performance of both foils in the array. Notably, an optimal range for a single foil's reduced frequency has been identified by several groups in the literature as $0.1 < f^* < 0.15$, lower than that of foils oscillating for propulsion. This was explored extensively by several groups including Kinsey & Dumas (2008), Simpson (2009) and Zhu (2011) and later Kim *et al.* (2017), who noted the role of f^* in stabilising the LEV formed on the foil during the high-velocity portion of its heaving cycle, resulting in increased performance. In an effort to combine the main parameters affecting the timing of wake interactions into a predictive quantity, Kinsey & Dumas (2012) proposed the global phase parameter. Their results only showed a consistent optimal global phase across cases with similar maximum effective angles of attack. They noted that their global phase lacked information about the wake velocity faced by the downstream foil, which led to different cases presenting a different optimal phase alignment. Xu & Xu (2017) studied configurations using potential flow theory and observed a different optimal phase from that of Kinsey and Dumas. Ribeiro *et al.* (2021) studied tandem arrays computationally and experimentally by separating different cases into wake regimes, a characterisation based on the maximum effective angle of attack and the structure of the wake behind the leading foil. In follow-up work, Ribeiro & Franck (2023) were able to identify and classify further wake patterns from simulation results of oscillating hydrofoil turbines through a machine learning approach. Su (2019) introduced a modified global phase parameter that, based on particle image velocimetry (PIV) measurements, incorporated a decelerated wake velocity with respect to the free stream. Ribeiro *et al.* (2021) similarly modified the global phase parameter from Kinsey & Dumas (2012) and proposed the wake phase parameter, given by

$$\Phi = 2\pi \frac{S_x}{u_p} f^* + \psi_{1-2}. \quad (1.1)$$

They showed that optimal phase alignment could be predicted across different tandem foil arrays. This parameter, which includes the average wake velocity within the swept distance directly upstream from the trailing foil, \bar{u}_p , to more accurately describe the mean flow speed between the two foils in the array, gives a sense of the alignment of the trailing foil with respect to primary wake structures. Rival, Hass & Tropea (2011) found two types of wake–foil interactions that resulted in either an increase or a decrease in the performance of the trailing foil. Ma *et al.* (2019) also showed how for a semi-passive system, negative vortex interactions had a more detrimental effect on system performance than the performance gained from favourable interactions. Zhao *et al.* (2023) did an experimental and numerical study of fully passive flapping foils in tandem configuration and found that the trailing foil always became ‘locked in’ by the wake generated from the leading foil, regardless of their initial states. They also found that the highest-efficiency cases saw the trailing foil heaving with a larger amplitude than that of the leading foil and displayed higher pitching velocities. Wang & Ng (2023) studied a semi-passive tandem foil array in which both foils were interconnected and operated with a spacing of $0.2c < S_x < 0.33c$ (where c is the foil’s chord length). They showed how the closely inter-connected foils could leverage constructive foil–foil interactions to improve their performance, and noted that this decreased separation improved the deployment density of the array. In very recent work, Ribeiro & Franck (2024) proposed a model to predict the efficiency of tandem foil arrays by relating the effective angle of attack and the change in instantaneous power output due to wake vortex interactions through the use of a coefficient of proportionality. They demonstrate that the model is able to predict direct vortex–foil impingement events as well as weak interactions of the trailing foil solely based on simulations of a single foil, although less accuracy is achieved at high-angle-of-attack wake regimes due to the increasing unsteadiness of the wake.

Previous studies have enforced the same kinematics on both foils in tandem arrays. Although this simplifies the parameter space required to seek optimal array configurations, enforcing single-foil optimal kinematics on all foils in the array might not lead to optimal system performance. The primary objective of this paper is to allow for the two foils to have different kinematics, to seek the settings that result in optimal collective energy-harvesting performance and to understand how the different foil kinematics within the array can result in improved wake–foil interactions. By prescribing the wake regimes identified by Ribeiro *et al.* (2021) (and further described by Ribeiro & Franck (2023)) through the kinematics of the leading foil, we evaluate the performance of the trailing foil within each wake regime over a large range of kinematic parameters. Performance is determined from force and torque measurements obtained through experiments performed in a water flume. An overview of the performance of all array configurations tested is presented, and a determination of which kinematic configuration of each foil results in the best-performing array is given. Finally, using the average power per cycle extracted from the array and flow measurements from PIV, comparisons are made between optimal and suboptimal cases to further investigate the effects of wake–foil interactions on the system.

2. Experimental methods

Figure 1 shows a diagram of the experimental set-up. Experiments were performed in an open-channel recirculating flume at Brown University with test section cross-section size of $0.8\text{ m} \times 0.6\text{ m}$ and 4 m in length. Two rectangular flat-plate hydrofoils were mounted vertically in the flow. Kim *et al.* (2017) tested multiple hydrofoils with different cross-sectional shapes and found that the shape of the foil did not have a significant influence on its energy-harvesting performance. Except where noted, the foils tested had a chord length

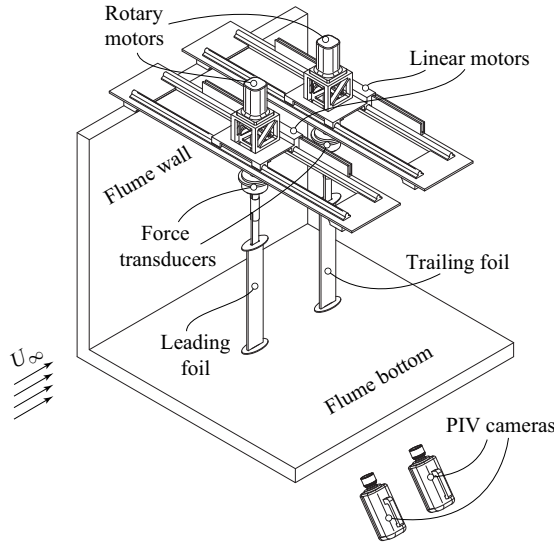


Figure 1. Experimental set-up.

of $c = 0.061$ m, a span of $b = 0.366$ m and were fitted with end plates extending $0.75c$ from the hydrofoil edge to their edge, which were used to suppress tip vortex effects. The heave and pitch motions of the hydrofoils were prescribed by using two gantry traverse systems controlled with servo motors (Parker rotary servo and AeroTech linear servo) mounted on the frame of the flume. The position of each hydrofoil was monitored independently using optical encoders (US Digital). Mounted between each traverse and foil, a six-axis force/torque transducer (ATI F/T Delta IP65) recorded force and torque at a sampling rate of 1000 Hz. The free-stream velocity was set at 0.33 m s^{-1} , measured with an acoustic Doppler velocimeter (Nortek Vectrino) positioned upstream, yielding a chord Reynolds number of $Re = 20\,000$. Water temperature was monitored during experiments and did not vary more than 1°C . At each experimental condition, (frequency, heave and pitch amplitude, etc.) measurements were taken for 40 oscillation cycles. The first and last five cycles were discarded to guard against any transients, and the middle 30 cycles were subsequently phase-averaged.

Two-component, time-resolved PIV measurements were acquired in an x - y plane located at the foil's mid-span. Two cameras (Photron Fastcam Nova R2, 2048×2048 pixels) were positioned below the test section, side by side, yielding a field of view measuring $0.25 \text{ m} \times 0.43 \text{ m}$. The flow field was illuminated using an Nd:YLF laser (Photonics Industries DM30) and image pairs were acquired at 200 Hz (approximately 310 flow fields for each foil oscillation cycle). The velocity fields were computed using DaVis v10 (LaVision). Velocity and vorticity fields were then phase-averaged over six oscillation cycles.

2.1. Oscillating hydrofoil kinematics and energy-harvesting performance

The main kinematic parameters governing the operation of the tandem hydrofoil array are shown in figure 2. The sinusoidal motion profiles of the hydrofoils are described by

$$h(t) = h_0 \sin(2\pi ft - \psi_{1-2}) \quad \text{and} \quad (2.1)$$

$$\theta(t) = \theta_0 \sin(2\pi ft - \pi/2 - \psi_{1-2}), \quad (2.2)$$

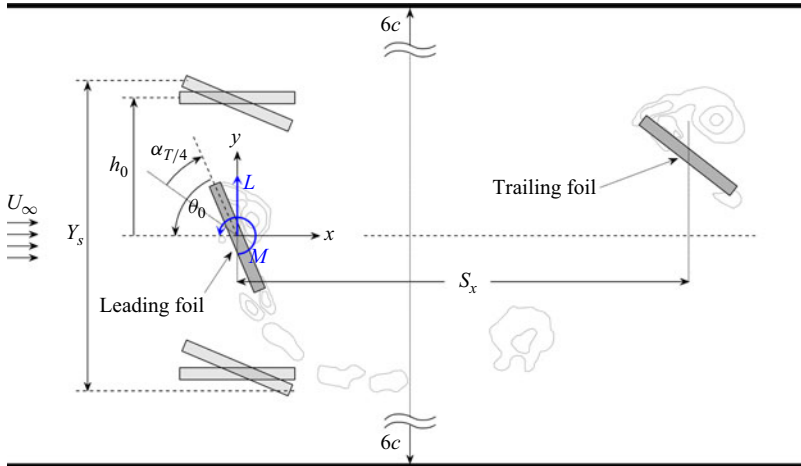


Figure 2. Top view of the measurement space, illustrating the kinematics of a tandem oscillating hydrofoil turbine. Shown are the pitching and heaving amplitudes, θ_0 and h_0 , respectively, the maximum effective angle of attack of the leading foil $\alpha_{T/4,le}$, the swept distance Y_s and the inter-foil separation S_x . Here $L(t)$ and $M(t)$ are the lift force and pitching moment and U_∞ is the free-stream velocity. The distance from the coordinate axis origin to the flume sidewalls in the transverse direction is 6 chord lengths.

where h_0 and θ_0 are the amplitudes of the heave and pitch motions, respectively, f is the frequency of oscillation in hertz, t is time in seconds and ψ_{1-2} is the phase between the motions of the leading and trailing foils. The phase between heaving and pitching motions was kept constant at $\pi/2$ based on the findings of Jones & Platzer (1997) and Jones, Lindsey & Platzer (2003), who investigated the relation of this parameter to propulsive and power extraction efficiency in OFTs.

We can relate a single foil's effective angle of attack, defined as

$$\alpha_{eff}(t) = \theta(t) - \tan^{-1}(\dot{h}(t)/U_\infty), \quad (2.3)$$

to the performance of the foil by using its maximum value, referred to $\alpha_{T/4}$ because it is the effective angle of attack at $t = T/4$, and which is defined as

$$\alpha_{max} \approx \alpha_{T/4} = \theta_0 - \tan^{-1}(2\pi h_0^* f^*), \quad (2.4)$$

where $h_0^* = h_0/c$ is the non-dimensional heave and $f^* = fc/U_\infty$ the reduced frequency (note that $\alpha_{T/4}$ values for the leading and trailing foils are indicated by the subscripts 'le' and 'tr', respectively). Previous studies (Kinsey & Dumas 2008; Simpson 2009; Kim *et al.* 2017; Ribeiro *et al.* 2021; Ribeiro & Franck 2023) have shown that $\alpha_{T/4}$ effectively parametrises the energy-harvesting performance of an oscillating foil.

The energy-harvesting performance of the hydrofoil is obtained from the sum of the power extracted due to the lift force, L , and the pitching moment, M :

$$P(t) = L(t)\dot{h}(t) + M(t)\dot{\theta}(t). \quad (2.5)$$

Energy-harvesting (or Betz) efficiency, η , is defined as the ratio between the power extracted per cycle by the foil and the power available in the oncoming flow:

$$\eta = \overline{P(t)}/0.5\rho U_\infty^3 A_s, \quad (2.6)$$

f^*	c/W	h_0	θ_0	$\alpha_{T/4}$
0.10	0.1, 0.07	0.5c–1.5c	40°–80°	0.02–0.96
0.12	0.1, 0.07	0.5c–1.5c	40°–80°	0.02–0.96
0.15	0.1, 0.07	0.5c–1.5c	40°–80°	0.02–0.96

Table 1. Single-foil experimental parameters explored in this study. Reduced frequency (f^*), heaving amplitude (h_0) and pitching amplitude (θ_0) were varied for foils with two different chord-to-test-section ratios, c/W . The combinations of parameters were selected to yield values of $\alpha_{T/4}$ ranging from 0.02 to 0.96 rad.

where ρ is the fluid density, A_s the swept area and $\overline{P(t)}$ is the cycle-averaged power. The swept area is calculated as $A_s = bY_s$, where

$$Y_s = \left[h(t) + \frac{c}{2} \sin(\theta(t)) \right]_{max} \quad (2.7)$$

is the swept distance, defined as the maximum distance travelled by the leading edge of the hydrofoil, and where c is the foil chord length and b its span. Note that the efficiency as defined by (2.6) is only valid for a foil facing a clean free stream. Although not employed in the current study, Ribeiro *et al.* (2021) re-defined η for the trailing foil in their tandem array by using an average wake velocity.

2.2. Blockage correction

Hydrofoil performance is affected by blockage effects due to experiments being performed in the flume which has sidewalls. We account for these effects using a blockage correction model from Maskell (1965), as implemented by Ross & Polagye (2020). This model couples axial momentum theory with assumptions about the wake behind a highly loaded turbine. Information on the bypass flow is required to make use of this correction, which, for this study, is obtained using the open-channel blockage correction model developed by Houlby, Draper & Oldfield (2008), as implemented by Ribeiro *et al.* (2021).

2.3. Kinematic parameter selection

Several series of experiments were conducted. In order to validate our system, we first characterised single-foil performance, measuring forces and torques over a range of frequencies, heave and pitch amplitudes (table 1). The single-foil-experiment parameters were chosen to yield $\alpha_{T/4}$ values ranging from 0.02 to 0.96 rad (as shown in figure 3). In addition, two foil sizes were tested with chord measuring 0.061 and 0.0762 m. The plates had thicknesses measuring 0.00635 and 0.0079 m, respectively, and had the same aspect ratio. The free-stream velocity was adjusted to preserve a constant Reynolds number (20000). Thus the only parameter changing was the ratio of chord to flume width, c/W .

Secondly, we conducted a parameter sweep study of the energy-harvesting performance (i.e. force/torque, no PIV) of tandem foils. In this series of measurements (table 2) we chose three leading-foil operating points representing the shear layer, LEV and LEV + TEV wake regimes (Ribeiro *et al.* 2021; Ribeiro & Franck 2023). As is discussed in § 3.1, these wake regimes each have an $\alpha_{T/4}$ range associated with it, and the chosen $\alpha_{T/4,le}$ lie within the range of each regime. The values selected for f^* were chosen to be near the single-foil optimum identified in the literature while allowing for two $\alpha_{T/4,le}$ combinations firmly within each wake regime and that are close in value. The choice of f^* additionally allows the investigation of the two performance branches identified by Ribeiro & Franck

Wake regime	$\alpha_{T/4,le}$	f^*	S_x	$h_{0,le}$	$\theta_{0,le}$	$h_{0,tr}$	$\theta_{0,tr}$	ψ_{1-2}
Shear layer	0.16	0.12	4c	0.8c	40°	{0.6c, 0.8c,	65°, 70°, 75°	{-110°, -52°,
Shear layer	0.16	0.12	6c	0.8c	40°	1.0c, 1.2c,	65°, 75°	0°, 52°,
Shear layer	0.18	0.11	4c	1.2c	50°	1.4c, 1.6c,	65°, 75°	110°, 180° }
LEV	0.33	0.12	4c	0.8c	50°	1.8c}	65°, 70°, 75°	
LEV	0.33	0.12	6c	0.8c	50°		65°, 75°	
LEV	0.35	0.11	4c	1.2c	60°		65°, 75°	
LEV + TEV	0.68	0.12	4c	0.8c	70°		65°, 70°, 75°	
LEV + TEV	0.68	0.12	6c	0.8c	70°		65°, 75°	
LEV + TEV	0.70	0.11	4c	1.2c	80°		65°, 75°	

Table 2. Tandem-foil experimental parameters explored in this study. The leading foil’s heaving ($h_{0,le}$) and pitching ($\theta_{0,le}$) amplitudes, as well as the reduced frequency (f^*) were set to obtain a desired $\alpha_{T/4,le}$ within each wake regime. Different combinations of inter-foil separation (S_x), inter-foil phase (ψ_{1-2}) and heaving ($h_{0,tr}$) and pitching ($\theta_{0,tr}$) amplitudes of the trailing foil were then tested.

Wake regime	$\alpha_{T/4,le}$	f^*	S_x	$h_{0,le}$	$\theta_{0,le}$	$h_{0,tr}$	$\theta_{0,tr}$	ψ_{1-2}
Shear layer	0.16	0.12	6c	0.8c	40°	0.7c	75°	60°, -120°
Shear layer	0.16	0.12	4c	0.8c	40°	0.8c, 1.2c	75°	0°
LEV	0.33	0.12	6c	0.8c	50°	0.7c	75°	60°, -120°
LEV	0.33	0.12	4c	0.8c	50°	0.8c	75°	60°
LEV	0.33	0.12	4c	0.8c	50°	1.4c	75°	-60°
LEV + TEV	0.68	0.12	6c	0.8c	70°	0.7c	75°	60°, -110°
LEV + TEV	0.68	0.12	6c	0.8c	70°	0.8c	75°	60°, -110°
LEV + TEV	0.68	0.12	4c	0.8c	70°	0.8c	75°	60°, 180°
LEV + TEV	0.68	0.12	4c	0.8c	70°	1.4c	75°	-110°, 180°

Table 3. Tandem-foil PIV experiments performed in this study. Wake regimes were prescribed by obtaining a desired $\alpha_{T/4,le}$ through the choice of the leading foil’s reduced frequency (f^*), heaving ($h_{0,le}$) and pitching ($\theta_{0,le}$) amplitudes. Then PIV was performed on selected combinations of trailing-foil heaving ($h_{0,tr}$) and pitching ($\theta_{0,tr}$) amplitudes, inter-foil separation (S_x) and inter-foil phase (ψ_{1-2}).

(2023) (also discussed in § 3.1). For each of the three leading-foil operating kinematics, a full parameter sweep of the trailing foil was performed by varying $h_{0,tr}$, $\theta_{0,tr}$, ψ_{1-2} , S_x and f^* , and the performance of the full system was quantified by calculating the power extracted by the tandem foil combination. The ranges selected for $h_{0,tr}$ and $\theta_{0,tr}$ were chosen to deviate significantly from the single-foil optimal combination found in the literature (Kinsey & Dumas 2008; Kim *et al.* 2017), while still encompassing said combination. The range in ψ_{1-2} allows for the exploration of a full range of phase configurations. The two separations S_x tested were chosen to explore the effect of placing the trailing foil closer upstream and having it interact with – presumably – stronger vortices shed by the leading foil. A total of 1323 combinations of kinematic parameters were tested.

Lastly, PIV was carried out for 16 parameter combinations – chosen to provide detailed flow information on the constructive and destructive wake–foil interactions identified during the full parameter sweep. The parameters for these cases are shown in table 3.

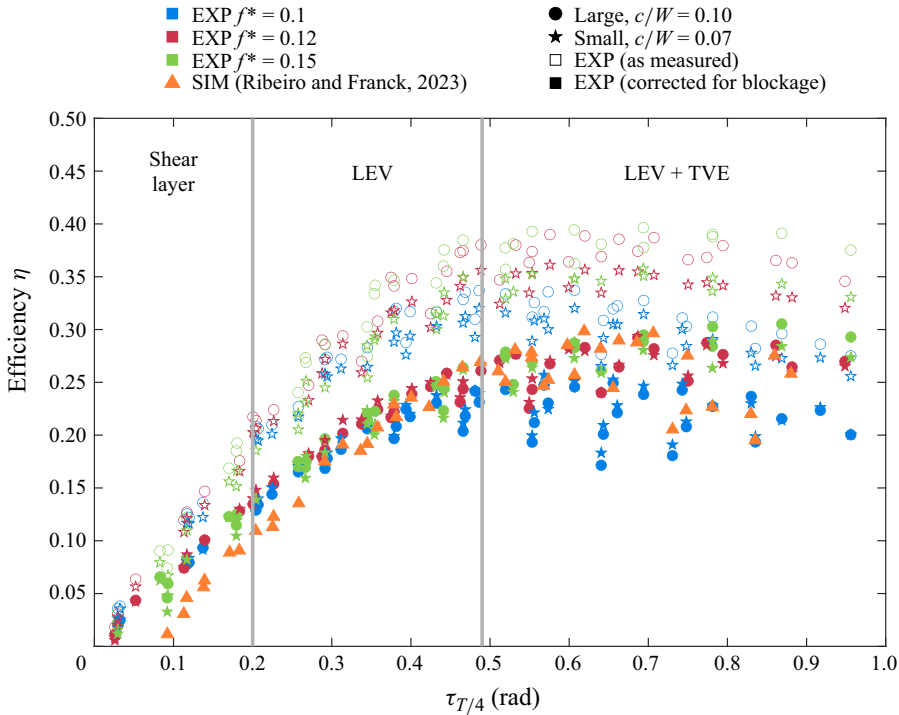


Figure 3. Energy-harvesting efficiency of a single foil as a function of its $\alpha_{T/4}$ value. Blue, red and green markers indicate different reduced frequencies. Orange triangle markers indicate simulation results from Ribeiro & Franck (2023). Circle and star markers correspond to the efficiency calculated from two differently scaled hydrofoils, where c/W is the ratio of the foil’s chord to the flume width. Overall, open markers indicate measured values and filled markers are blockage-corrected values (Maskell 1965; Ross & Polagye 2020).

3. Results and discussion

3.1. Single-foil performance and blockage correction

Figure 3 shows the Betz efficiency, η , of a single foil as a function of $\alpha_{T/4}$ measured over a range of frequencies, pitch and heave amplitudes and blockage, c/W (table 1). Several features should be noted. Firstly we see that the efficiency of the larger foil ($c/W = 0.10$, open circle markers) is higher than that of the smaller foil ($c/W = 0.07$, open star markers) and that the performance of both foils decreases and almost perfectly collapses onto a single curve once the blockage correction is applied (filled circle and star markers). With the blockage correction applied, both sets of experimental data agree very well with the computations of Ribeiro & Franck (2023) (filled orange triangle markers), which were performed for an elliptical foil in an infinite (unconstrained) domain.

Secondly, once the blockage correction is applied (filled symbols) there is excellent scaling of η within the shear-layer and LEV regimes ($\alpha_{T/4} < 0.5$), while in the LEV + TEV regime ($\alpha_{T/4} > 0.5$) we see the efficiency spread out with the lower frequencies (blue symbols) exhibiting a lower efficiency than the higher frequencies (red and green symbols). This behaviour agrees with the computations of Ribeiro & Franck (2023) (orange symbols), who also observed this bifurcation, and remarked that the split in the $\alpha_{T/4}$ scaling in the LEV + TEV regime divided according to the frequency, with the upper branch corresponding to cases with $f^* = 0.15$ and $f^* = 0.12$, while the lower branch corresponded to cases with a lower frequency, $f^* = 0.1$.

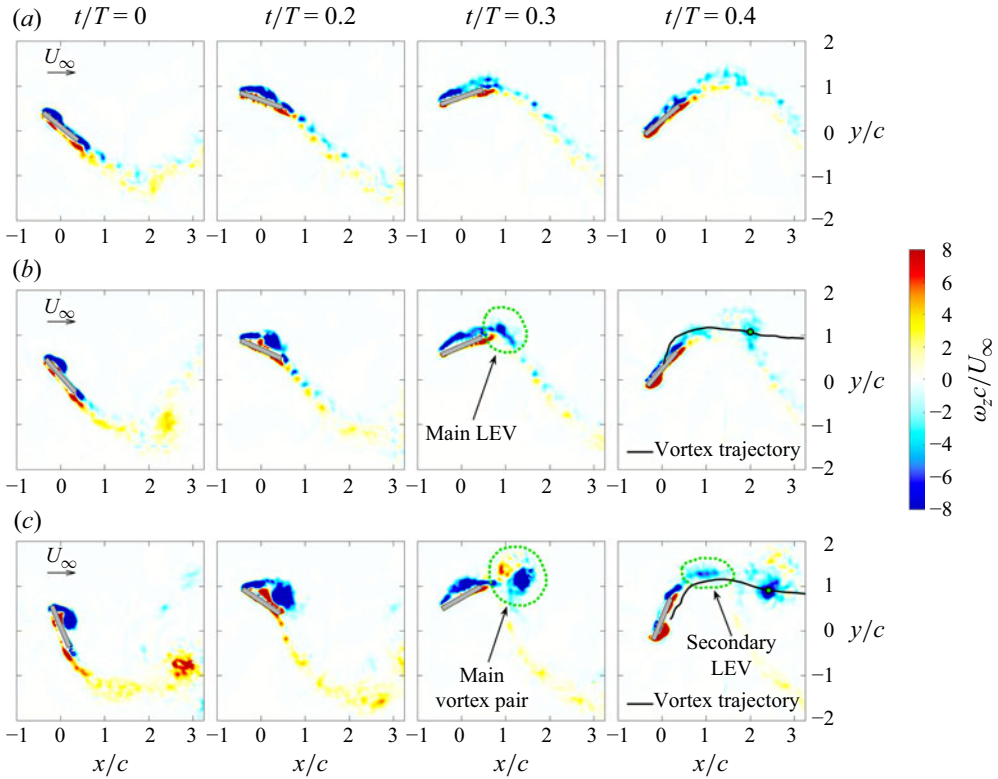


Figure 4. Contours of vorticity for each wake regime at different times within an oscillation cycle. In all three cases the leading foil’s reduced frequency is $f^* = 0.12$ and its heaving amplitude is $h_{0,le} = 0.8c$. (a) The shear-layer regime, $\alpha_{T/4,le} = 0.16$, $\theta_{0,le} = 40^\circ$. (b) The LEV regime, $\alpha_{T/4,le} = 0.33$, $\theta_{0,le} = 50^\circ$. (c) The LEV + TEV regime, $\alpha_{T/4,le} = 0.68$, $\theta_{0,le} = 70^\circ$. The main vortices in the LEV and LEV + TEV regimes are highlighted in the last snapshot, as well as the trajectory of the primary vortex. The small green circle marker in the fourth panel of each wake regime ($t/T = 0.4$) indicates the location of the vortex core at that instance.

3.2. Wake structure and vortex trajectories behind a single hydrofoil

The three wake regimes identified by Ribeiro *et al.* (2021) are confirmed by PIV measurements behind the leading foil, and are shown in figure 4 at four times during the cycle. At the lowest angles of attack, over a range of $0 < \alpha_{T/4,le} \leq 0.2$, the ‘shear-layer regime’ is characterised by a shear layer in the wake with only weak vortex formation. At intermediate angles of attack, we can identify the ‘leading edge vortex regime’ (LEV regime) at values of $0.2 < \alpha_{T/4,le} \leq 0.49$. Lee *et al.* (2022) showed how the primary LEV shed by the foil in this regime is advected downstream in a mostly straight downstream direction from its detachment location. This behaviour is confirmed by the vortex path shown in the last panel of figure 4(b). The highest range of $\alpha_{T/4,le}$ denotes the ‘leading edge vortex + trailing edge vortex regime’ (LEV + TEV) which sees a vortex pair shed by the foil every stroke. The primary LEV is stronger and larger than in the other wake regimes and is accompanied by a small counter-rotating TEV. Lee *et al.* (2022) also showed that the orbiting interaction between these two vortices in this regime results in a curved trajectory as the vortex pair travels downstream (figure 4c; $t/T = 0.4$).

Figure 5(a–c) shows the wake velocity averaged over all snapshots, \bar{u}_{wake} , behind the leading foil for each wake regime. These results, which align closely with those reported

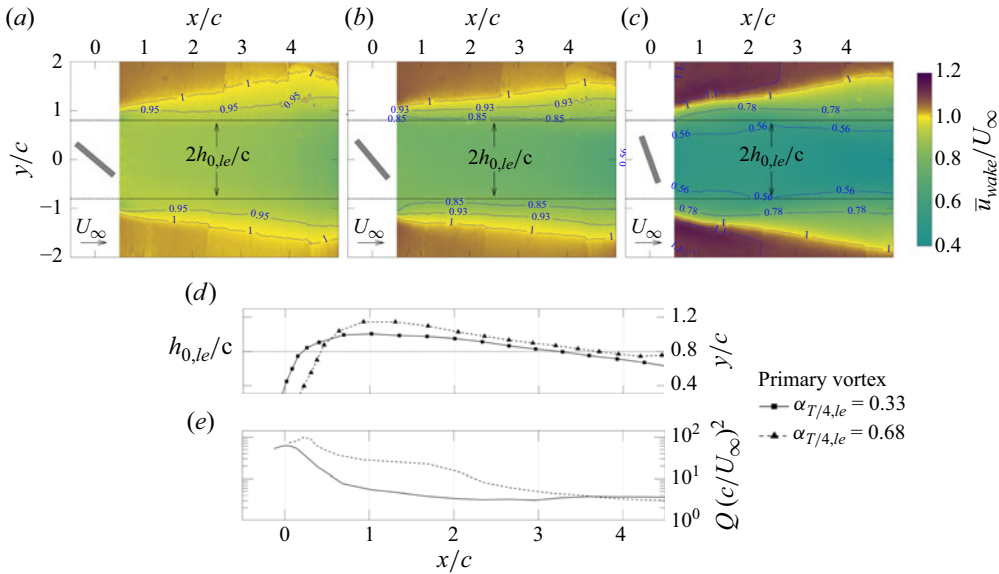


Figure 5. (a–c) The averaged wake velocity, \bar{u}_{wake} , calculated from PIV measurements for each wake regime, obtained from time-averaging the instantaneous wake velocity over 10 oscillation cycles. The three cases presented have the same $\alpha_{T/4,le}$ values as those presented in figure 4, i.e. (a) 0.16, (b) 0.33 and (c) 0.68 rad. Also shown are the (d) trajectory and the (e) Q -value of the primary vortex in the LEV and the LEV + TEV regimes.

by Ribeiro *et al.* (2021), show how the wake velocity within the confines of the leading foil’s heaving amplitude decreases at higher values of $\alpha_{T/4,le}$. The leading foil’s heaving amplitude is fixed at $h_{0,le} = 0.8c$ in all wake regimes, setting the shedding location of the primary LEV. Although the trajectory of the primary LEV is slightly different in both wake regimes, the vortex remains within the same y/c region as it nears the position of the trailing foil. Due to the presence of the strong vortices, this region in the wake is characterised by high turbulent kinetic energy, as shown by Ribeiro *et al.* (2021), which defines a sort of boundary of the pure deficit region. Figures 5(d) and 5(e) show the main vortex trajectory and Q -value, where Q is the second invariant of the velocity gradient tensor,

$$Q = \frac{1}{2} \left(\|\boldsymbol{\Omega}\|^2 - \|\mathbf{S}\|^2 \right), \quad (3.1)$$

for the two wake regimes with prominent vortex structures, where $\boldsymbol{\Omega}$ is the rotation-rate tensor and \mathbf{S} the strain-rate tensor. It can be inferred from figure 5 that $h_{0,le}$ indirectly affects the optimal choice $h_{0,tr}$, as it defines the region of decelerated flow in which the trailing foil will have to operate.

3.3. Array performance

It would seem logical to assess the performance of the tandem array through the Betz efficiency (2.3) as with the single-foil results presented in figure 3. The problem arises in choosing the appropriate scale of energy available to both foils in the array. Several factors complicate the choice of efficiency metric: the large difference in flow windows for each foil, the wake deficit region and bypass flow region, the presence of strong wake vortices that result in either better or worse trailing-foil performance and the increasingly unsteady character of the wake at higher $\alpha_{T/4,le}$ ranges. An array efficiency

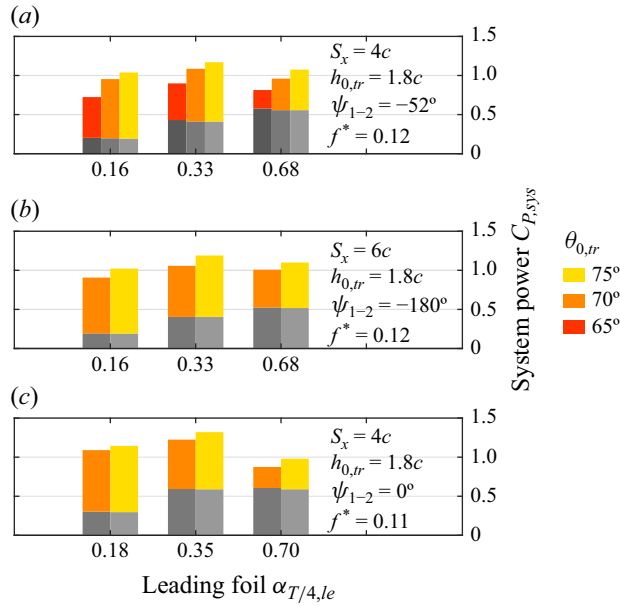


Figure 6. Power extracted by the system as a function of the trailing-foil pitch amplitude $\theta_{0,tr}$. The grey bars are the power extracted by the leading foil, while the coloured bars are the power from the trailing foil.

would require information on both foils’ kinematic configuration as well as the effects of wake–foil interactions. This was addressed by Ribeiro *et al.* (2021) with a rescaled trailing-foil efficiency that incorporated the energy from the mean wake flow and the turbulent kinetic energy. While this modified efficiency provides a more complete picture of the performance of the array, the reliance on flow measurements to obtain this modified efficiency makes it unsuitable for systematically evaluating the performance of configurations where the trailing foil has a large range of different kinematics. The predictive model subsequently proposed by Ribeiro & Franck (2024) could offer a simplified approach, where the predicted trailing-foil efficiency could be used to rescale the power obtained from it and finally using the result along with the leading foil’s power to obtain a system-wide efficiency. In this study, however, we focus only on the cumulative power of the two foils as it allows us to assess the effective performance of the array and simplify the array analysis, while still making the primary effects of wake–foil interactions evident.

Figures 6–8 present a cross-sectional overview of the system power extraction results of the two-foil tandem array. The total power coefficient of the system is given by

$$C_{P,sys} = \frac{\overline{P_{le}(t)} + \overline{P_{tr}(t)}}{0.5\rho U_{\infty}^3 cb}, \quad (3.2)$$

and each figure shows the variation of the system power as a function of different parameter combinations for the array. Within each figure, there are three sub-figures, each representing a different sampling of the trailing-foil parameters. Each sub-figure contains three groups of power coefficients representing the shear-layer, LEV and LEV + TEV regimes, defined by three values of $\alpha_{T/4,le}$. Lastly, in each group of C_P plots, a bar-graph ‘stack’ is shown in which a specific parameter is systematically varied: $\theta_{0,tr}$, $h_{0,tr}$ and ψ_{1-2} (figures 6, 7 and 8, respectively). Each bar-graph stack shows the leading-foil $C_{P,le}$ in grey

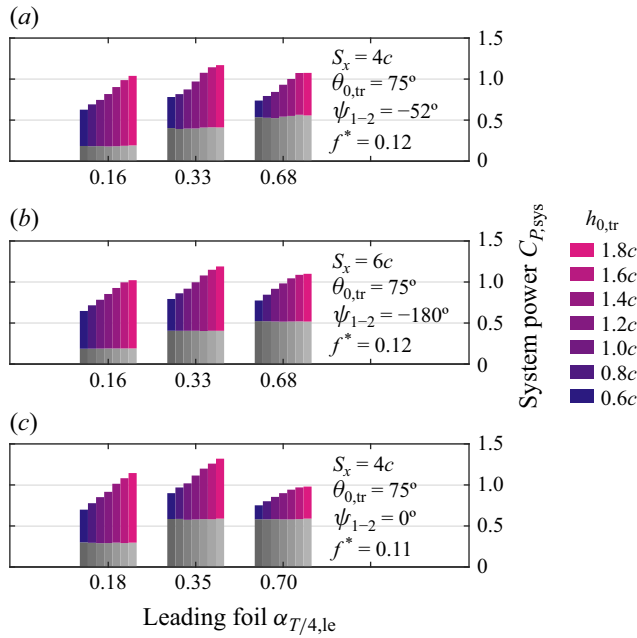


Figure 7. Power extracted by the system as a function of the trailing-foil heave amplitude $h_{0,tr}$. The grey bars are the power extracted by the leading foil, while the coloured bars are the power from the trailing foil.

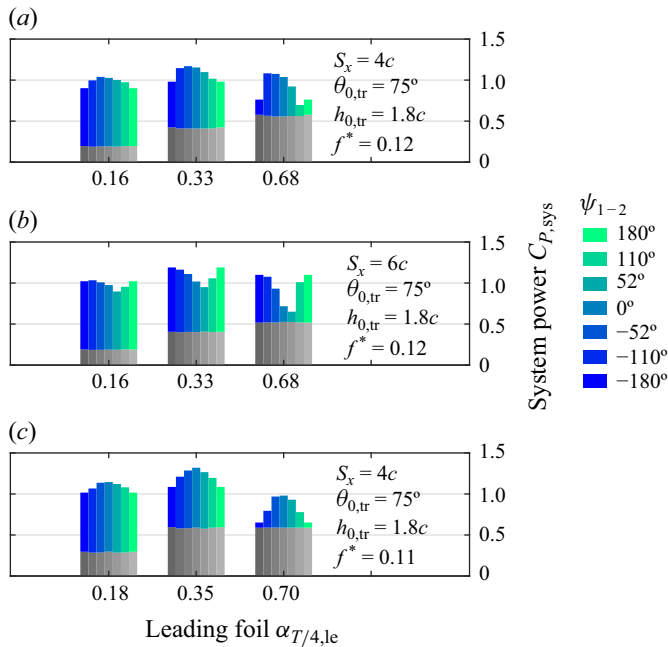


Figure 8. Power extracted by the system as a function of inter-foil phase ψ_{12} . The grey bars are the power extracted by the leading foil, while the coloured bars are the power from the trailing foil.

(which is more-or-less constant within each group, since the leading-foil kinematics are fixed for that group); the trailing-foil performance, $C_{P,tr}$, is shown in colour.

Results from Kinsey & Dumas (2012) and Xu, Sun & Tan (2016) identified that S_x mainly affects the timing of wake–foil interactions. And while other parameters like f^* and ψ_{1-2} also affect directly these interactions, S_x further influences the energy extracted by the downstream foil due to the wake velocity deficit. Figures 6(a,b), 7(a,b) and 8(a,b) correspond to cases that have the same $\alpha_{T/4,le}$ values but different inter-foil separations ($S_x = 4c$ in (a) and $6c$ in (b)); therefore the only parameter changing is S_x (at optimal phasing, ψ_{1-2}). We observe that the magnitude of $C_{P,sys}$ does not vary significantly due to S_x , which we can explain with figure 5(a–c), where it is observed that the wake velocity does not recover very much between these two separations in all wake regimes, and thus the trailing foil faces approximately the same decreased upstream flow velocity for both separations tested. Considering the negligible variation of wake velocity for the tested S_x , it might be desirable to space the foils closely to increase the number of turbines deployed in a given area, i.e. the power density of the array. As shown by figure 5(e), decreasing S_x would ensure that vortices being shed from the leading foil are stronger and more coherent, and therefore could be harnessed by the trailing foil more effectively. However, this also means that strong negative vortex–foil interactions could also occur, making optimising the array kinematics all the more important. It is important to note that decreased leading-foil performance can result from spacing the foils closer together, as observed by Xu *et al.* (2016), who noted that the blockage effect of the trailing foil on the leading foil becomes more important at these close separations. This detrimental effect was also shown by Zhao *et al.* (2023) in their passive system who found that as S_x is decreased near $2c$, the trailing foil’s influence on the leading foil can lead to decreased leading-foil performance.

Figure 6 demonstrates that increases in the trailing-foil pitch amplitude, $\theta_{0,tr}$, correlate with increased trailing-foil performance. As proposed by Ribeiro *et al.* (2021), we consider an effective wake velocity, \bar{u}_{eff} , for the trailing foil given by integrating the time-averaged wake velocity (\bar{u}_{wake}) within the swept area lc upstream of the trailing foil. This can be used to rescale f_{tr}^* and $\alpha_{T/4,tr}$. Therefore, although the physical frequency is fixed for both foils in the array, the trailing foil’s effective non-dimensional frequency is increased with respect to the leading foil’s according to $f_{tr}^* = fc/\bar{u}_{eff}$, due to the diminished velocity faced by the trailing foil with respect to the leading foil (see figure 5a–c). In their single-foil experiments Kim *et al.* (2017) showed that the optimal pitch amplitude rises as f^* is increased, and this same trend was observed in the numerical simulations of Kinsey & Dumas (2008). This effect can be explained by observing that the relative speed between the oncoming flow and the trailing foil is lower (leading to the increased f_{tr}^* relative to f^*) which, by rescaling (2.4) with \bar{u}_{eff} ,

$$\alpha_{T/4,tr} = \theta_{0,tr} - \tan^{-1} (2\pi h_{tr}^* f_{tr}^*) = \theta_{0,tr} - \tan^{-1} \left(2\pi h_{tr}^* \left(\frac{fc}{\bar{u}_{eff}} \right) \right), \quad (3.3)$$

results in a lower maximum effective angle of attack. This can then be compensated for by a shift of the optimal $\theta_{0,tr}$ towards higher amplitudes, possibly beyond the maximum value tested (75°) in this sequence of experiments.

Figure 7 presents the system performance dependency on the trailing-foil heave amplitude and demonstrates that the performance of the trailing foil rises with increasing $h_{0,tr}$ in all three wake regimes. This was also observed for a single foil by Kinsey & Dumas (2008), and although their work focused on the efficiency of the foil (which is scaled by the swept area; see (2.6)), they remarked that by increasing the foil’s h_0 a higher C_P (which is scaled by the foil’s surface area) was obtained despite a lower efficiency. Additionally, by

allowing $h_{0,tr}$ to be much larger than $h_{0,le}$, the trailing foil can access higher momentum fluid and thus improve its $C_{P,tr}$. Note how [figure 5](#) shows an increase in the amplitude of the bypass flow behind the leading foil, most notably in the LEV + TEV regime where it reaches up to $\bar{u}_{wake}/U_\infty \sim 1.1$. As with the pitch amplitude discussion earlier, it is possible that our test matrix did not explore sufficiently large values of $h_{0,tr}$, although the incremental improvement does seem to be flattening out. Interestingly, [Zhao *et al.* \(2023\)](#) also found that the best performance of the trailing foil was achieved for higher heaving and pitching amplitudes at inter-foil separations ranging from $S_x = 1c$ to $6c$, even though they had a fully passive system. Notably, the local $C_{P,tr}$ maximum is only reached at the LEV + TEV wake regime at $h_{0,tr} = 1.6c$, after which it plateaus. One possible reason for this is that the more unsteady wake of the LEV + TEV regime limits the power extraction of the trailing foil at very high $h_{0,tr}$ due to the presence of strong vortices in this region.

The performance variations of the trailing foil with respect to changing the inter-foil phase, ψ_{1-2} , are presented in [figure 8](#). Many studies ([Ashraf *et al.* 2011](#); [Kinsey & Dumas 2012](#); [Karakas & Fenercioglu 2017](#); [Ribeiro *et al.* 2021](#)) have explored the effect of this critical parameter on the performance of the array. For foils sharing the same f^* , θ_0 and h_0 , [Ribeiro *et al.* \(2021\)](#) evaluated the tandem array's performance for a large range of ψ_{1-2} and observed the same harmonic trends that [figure 8](#) demonstrates. The effect of ψ_{1-2} becomes more pronounced as $\alpha_{T/4,le}$ is increased due to the stronger wake features, leading to variations of different magnitude in $C_{P,tr}$ for each wake regime (± 0.05 in the shear-layer regime and ± 0.25 in the LEV + TEV regime). The timing of wake-foil interactions, dictated mainly by ψ_{1-2} , will lead to optimal or suboptimal parameter combinations, which can be more easily identified by using the wake phase parameter, Φ , from [Ribeiro *et al.* \(2021\) \(1.1\)](#).

[Figure 9\(a\)](#) presents cases in the LEV + TEV regime over a range of trailing-foil heave, $h_{0,tr}$, and foil separation, S_x , scaled using the wake phase parameter. We observe that, while cases with low performance fall in a clear trough at $\Phi = 90^\circ$, high-performance cases fall within a much wider Φ envelope spanning a range of -180° to 0° . Although this optimal range is rather flat, most of the cases shown have an optimal wake phase of $\Phi = -90^\circ$, with a slight negative shift at higher $h_{0,tr}$, which seems to indicate that the phase relationship between the trailing foil and the wake is sensitive to having a larger trailing-foil heaving amplitude than that of the leading. Although not shown, cases in the LEV regime show the worst-performing configurations at a value of $\Phi = 0^\circ$, and an envelope of high-performance cases at $|\Phi| > 90^\circ$. This same trend is observed less clearly in the shear-layer regime due to weaker wake-foil interactions, and additionally display a small negative phase shift. Although our results for the two lowest $\alpha_{T/4,le}$ regimes align with those reported by [Ribeiro *et al.* \(2021\)](#), there is a notable difference in the LEV + TEV regime, where they found an optimal value of $\Phi = 120^\circ$. This suggests that due to the increased unsteadiness of the wake in the LEV + TEV regime, additional considerations are required to characterise the wake's wavelength such as incorporating the primary LEV's advection speed and trajectory. This echoes the results from [Ribeiro & Franck \(2024\)](#) who noted that their performance prediction model for tandem foil arrays (which relies on Φ) showed decreased accuracy for cases in the LEV + TEV regime (especially near the values tested in this study), possibly due to the presence of additional wake vortices and an increasingly complex wake structure. As shown in [figure 4\(c\)](#), there is a significant secondary LEV in the LEV + TEV regime that can potentially affect the trailing foil's performance, along with the TEV accompanying the primary LEV. Although not explored in the current study, further modifications of the wake phase could incorporate effects of these additional wake vortices.

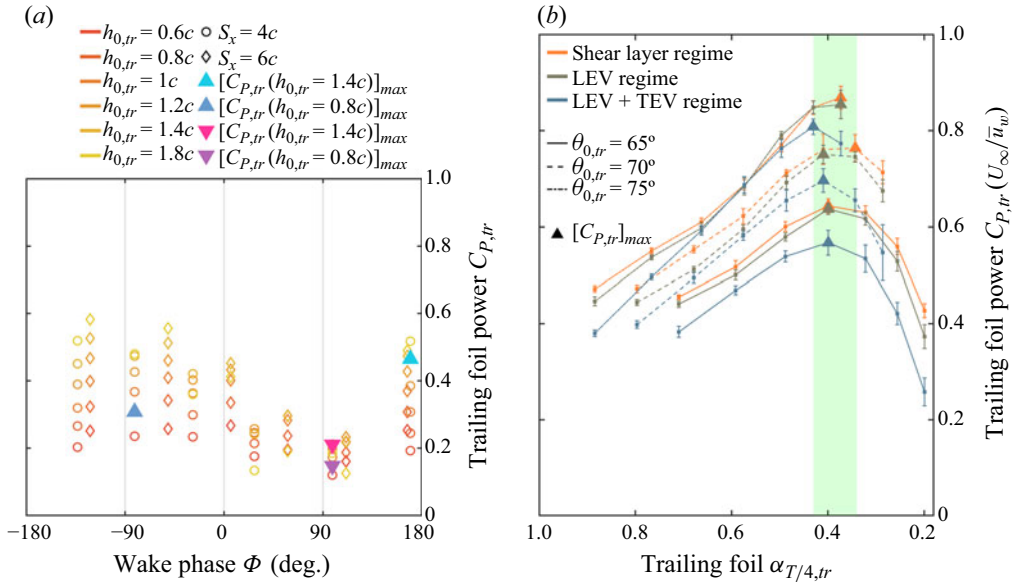


Figure 9. (a) Power extracted by the trailing foil for different kinematic configurations within the LEV + TEV wake regime as a function of the wake phase parameter Φ from Ribeiro *et al.* (2021). The cases highlighted by Δ markers and ∇ markers demonstrate constructive and destructive interactions, respectively, and are analysed with PIV in § 3.5. (b) Power extracted by the trailing foil at optimal values of Φ for each wake regime, for a range of $\theta_{0,tr}$, and with maximum $C_{P,tr}$ values highlighted for each $\theta_{0,tr}$. Data are scaled using the trailing foil’s $\alpha_{T/4,tr}$ and with the effective wake velocity, \bar{u}_{eff} , where it is observed that maximum values of $C_{P,tr}$ fall within a range of $0.32 < \alpha_{T/4,tr} < 0.41$ rad, highlighted in green.

As observed by Ashraf *et al.* (2011) and Kinsey & Dumas (2012), some types of wake–foil interactions can lead to dramatically improved performance of the trailing foil. As is explained in § 3.5, unexpectedly better performance can be obtained from the trailing foil due to favourable interactions with wake vortices. These types of interactions were also captured by the results of Ribeiro & Franck (2024), where for the higher $\alpha_{T/4}$ values tested (0.4 and 0.49 rad) their model predicted vortex–foil interactions that led to significant increases in power output due to lift. A similar conclusion can be obtained from looking at figure 8, as it is apparent that the large variation in performance in the LEV + TEV regime (where wake–foil interactions are presumed to be most influential) results in a system that is strongly affected by small changes in ψ_{1-2} . From a practical perspective, it may be beneficial to operate within the LEV regime so that the trailing foil engages in weaker wake–foil interactions, yielding a more robust performance as well as slightly better system performance at the optimal operating kinematics.

We note that an $\alpha_{T/4,tr}$ scaling of across all wake regimes can be found for the performance of the trailing foil. Figure 9(b) shows cases with different trailing-foil heave and pitch, $h_{0,tr}$ and $\theta_{0,tr}$, but equal wake phase, Φ . As previously discussed, optimal values of Φ vary among all wake regimes. As indicated by the literature (Ma *et al.* 2019; Ribeiro *et al.* 2021; Ribeiro & Franck 2024), if we assume that vortex–foil interactions generally result in poor trailing foil performance, this would indicate that for optimal values of Φ cases would display weaker wake–foil interactions across wake regimes. Therefore, cases shown in figure 9(b) are chosen to be within the optimal range of Φ of their respective wake regime. This also ensures that potentially strong vortex–foil interactions do not introduce additional variability. By additionally scaling $C_{P,tr}$ using the mean wake velocity, \bar{u}_{eff} , figure 9(b) demonstrates how the performance of the trailing foil scales with $\alpha_{T/4,tr}$ when

subjected to similar upstream conditions. By noting that increasing $\theta_{0,tr}$ shifts up the optimal value of $h_{0,tr}$ for all wake regimes, it follows that larger $h_{0,tr}$ at a fixed frequency increases \dot{h}_{tr} and therefore the power due to lift, $P_L = L\dot{h}_{tr}$. However, the trailing foil's effective angle of attack, $\alpha_{eff,tr}$, will decrease (2.3) as \dot{h}_{tr} increases, acting to reduce the lift generated by the foil. This is countered by raising $\theta_{0,tr}$ to increase $\alpha_{eff,tr}$ and subsequently the lift, therefore obtaining higher power extraction. Three key findings can be found from these results. The first is that there is an optimal range of $\alpha_{T/4,tr}$ for all wake regimes at $0.32 < \alpha_{T/4,tr} < 0.41$, indicating that the effective angle of attack remains useful to parametrise the performance of multiple foils within an array. Secondly, the difference in trailing-foil performance between the shear-layer and LEV regimes can be described primarily by the wake deficit, indicated by the collapse of their performance into a single curve for each $\theta_{0,tr}$. Finally, while the trailing foil's performance within the LEV + TEV regime with an optimal Φ and the highest $\theta_{0,tr}$ tested (75°) aligns with that of the shear-layer and LEV regimes, for the other two $\theta_{0,tr}$ tested (65° and 70°) it deviates significantly. This is further evidence that the trailing foil's performance within the LEV + TEV regime is complicated by the increased unsteadiness in this regime.

3.4. Optimal system performance

It is interesting to recognise from all of these results (figures 6–8) that the maximum system power extracted is obtained from the LEV wake regime ($\alpha_{T/4,le} \sim 0.35$). In this case, even though the leading foil is not operating at its maximum capacity, the wake has more energy available for the trailing foil to capture and the system performance is maximised. Furthermore, the global optimum across all parameter combinations tested corresponds to the LEV regime with both foils operating with $f^* = 0.11$. Figure 3 shows that a single foil's maximum energy-harvesting efficiency can be achieved at $f^* > 0.11$ when operating within the LEV + TEV regime. In the tandem array, when the leading foil operates in the LEV regime, the $\alpha_{T/4,le}$ value for the $f^* = 0.11$ cases is slightly higher than for the $f^* = 0.12$ cases (0.35 versus 0.33 rad, respectively), which accounts for the increase in performance of the leading foil. Recall the performance bifurcation identified by Ribeiro & Franck (2023) for higher $\alpha_{T/4}$ values, and that the lower branch in this bifurcation corresponds to $f^* \sim 0.11$. Cases with $f^* = 0.11$ place the leading foil in that lower-performance branch when operating in the LEV + TEV regime, explaining the notable drop in its performance with respect to cases with $f^* = 0.12$. Ultimately this results in significantly worse system performance within the LEV + TEV regime for the $f^* = 0.11$ cases.

3.5. Constructive and destructive vortex–foil interactions

The system power performance results do not directly explain why some wake–foil interactions enhance trailing-foil performance, while other kinematic choices degrade the trailing-foil performance. Ashraf *et al.* (2011), Kinsey & Dumas (2012), Xu *et al.* (2016) and Karakas & Fenercioglu (2017) identified some types of interactions that led to better or worse trailing-foil performance. However, in their tests both foils in the array shared the same heaving amplitude. In the present study, due to the large differences in heave amplitude between the leading and trailing foils, the wake phase parameter by itself does not make it immediately apparent what types of wake–foil interactions lead to high- and low-performance cases.

Detailed analysis of the four cases highlighted in figure 9(a) illustrates how certain kinematics, specifically ψ_{1-2} and $h_{0,tr}$, lead to improvements in performance. We consider constructive interactions between the wake and the trailing foil as those

that lead to improved trailing-foil performance (two up-facing triangle markers), while destructive interactions (two down-facing triangle markers) are those resulting in decreased performance. These cases are evaluated within the LEV + TEV regime so that wake–foil interactions are amplified due to the stronger vortices in the wake when compared with the lower $\alpha_{T/4,le}$ regimes. Furthermore, this analysis is done at the shortest separation tested ($S_x = 4c$) since it is assumed that wake vortices are stronger than when they are further downstream.

Two pairs of constructive and destructive interactions are compared in [figures 10](#) and [11](#). Each figure shows snapshots from the PIV-measured flow field taken at four instances in time (A–D) during half of the trailing foil’s oscillation cycle. In both figures, the colour shading represents the local dynamic pressure normalised by the free-stream dynamic pressure, q^* :

$$q^* = (|\mathbf{u}|/U_\infty)^2, \tag{3.4}$$

where $|\mathbf{u}|$ is the instantaneous velocity field magnitude at each snapshot. Note that variations in q^* are primarily due to the vortex-induced velocity. This metric allows us to determine when the trailing foil operates in more or less energetic regions of the wake, which we can relate to increases or decreases in the foil’s energy-harvesting performance. Instantaneous streamlines are shown to provide a sense of the direction of the flow. Thick black contour lines represent isolines of Q ([3.1](#)), non-dimensionalised appropriately: $Q(c/U_\infty)^2 = 1.5$ (note that q^* and Q represent different quantities). These contour lines visualise the location of strong vortices in the wake. Below the q^* fields, the corresponding instantaneous effective angle of attack α_{eff} , lift coefficient C_L , moment coefficient C_M and power coefficient C_P curves of the trailing foil are shown for both the constructive (blue line) and destructive (purple line) cases.

The maximum and minimum $C_{P,tr}$ cases at $h_{0,tr} = 0.8c$ are presented as constructive and destructive interactions in [figures 10\(a\)](#) and [10\(b\)](#), respectively. In this configuration, both foils are exposed to the same flow window. The trailing foil operates only within the pure wake deficit region, which can be observed from the snapshots presented in [figure 10\(a,b\)](#), showing the foil positioned within the blue-shaded region in all snapshots. In the constructive case, shown in [figure 10\(a\)](#), the trailing foil extracts an average power of $\overline{C_{P,tr}} = 0.299$ per cycle (blue Δ marker in [figure 9a](#)), while the destructive case in [figure 10\(b\)](#) results in $\overline{C_{P,tr}} = 0.138$ (purple ∇ marker in [figure 9a](#)). These first two cases are of interest as they see the leading and trailing foils heaving with the same amplitude, and their wake phase, Φ , is separated by 180° (-90° for the constructive and 90° for destructive; see [figure 9a](#)). Here, the choice of ψ_{1-2} results in the trailing foil performing better due to its avoidance of wake vortices. This can be observed in the PIV snapshots in [figure 10\(a\)](#), whereby following the primary LEV in the wake (large circle on the top left in snapshot A), we observe how the trailing foil avoids it as it travels downstream throughout the subsequent snapshots. This is in contrast to the destructive case where, as observed in snapshots B and C in [figure 10\(b\)](#), the trailing foil collides head-on with the wake LEV. Due to the lack of strong vortex–foil interactions, the constructive case would be considered a weak interaction as described by Kinsey & Dumas ([2012](#)) and Xu *et al.* ([2016](#)), while the direct collision with vortical structures in the destructive case makes it a strong wake interaction case.

The difference in performance between these two cases is primarily due to the effective angle of attack that the trailing foil experiences during its oscillation ([figure 10d](#)). There is a large difference in α_{eff} during instances A and B. By looking at the flow direction faced by the trailing foil in these two snapshots, we observe that the destructive case ([figure 10b](#),

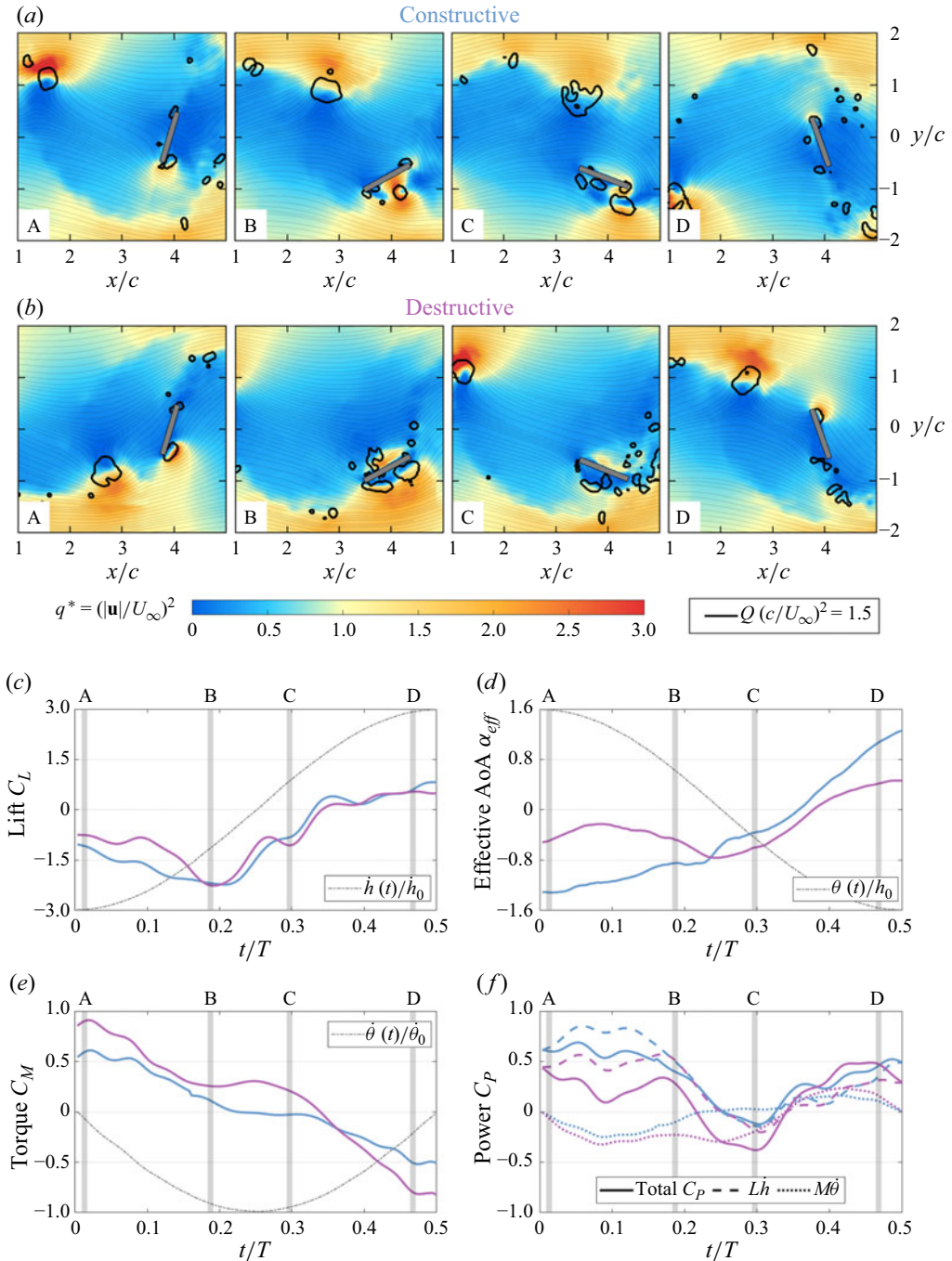


Figure 10. Snapshots of dynamic pressure $q^* = (|\mathbf{u}|/U_\infty)^2$, with instantaneous streamlines of wake-foil interactions for $S_x = 4c$, $\alpha_{T/4,le} = 0.68$, $\theta_{0,tr} = 75^\circ$ and $h_{0,tr} = 0.8c$. Isolines of $Q(c/U_\infty)^2 = 1.5$ are shown to visualise primary vortices. Cases shown are for two values of inter-foil phase: (a) $\psi_{1-2} = 51^\circ$ for the constructive case and (b) $\psi_{1-2} = 180^\circ$ for the destructive case. Also shown are non-dimensional (c) lift, (d) torque, (e) effective angle of attack and (f) power over half of an oscillation cycle. Also shown in (f) are the power contributions from lift and torque.

A–B) sees the trailing foil's α_{eff} lowered because of the flow induced by the vortex shed from the leading foil (high Q contour). This behaviour was also observed by Kinsey & Dumas (2012) in their 'v4' classification of wake–foil interactions. In contrast, snapshots A and B of the constructive case (figure 10a) show that the foil experiences a sustained high α_{eff} (figure 10d, A–B). This results in higher lift (figure 10c, A–B) at this initial part of the cycle. This difference in lift has a significant impact on performance due to the high heaving velocity of the foil at this time that, because of its alignment with C_L , yields a high contribution to the power extracted (figure 10f, A–B).

Turning attention to the stroke reversal (B–C in figure 10), in the constructive case, we observe minimal torque and power from the LEV as it moves over the foil towards the trailing edge (figure 10a,e,f, B–C). In contrast, the destructive case sees the attached LEV partially suppressed due to its collision with the wake LEV (figure 10b, B–C) which results in a positive torque (figure 10e, B–C) and a negative contribution to power (figure 10f, B–C). Over the entire cycle, most of the energy extraction (figure 10f) comes from lift production – in agreement with Xu *et al.* (2016) and Kim *et al.* (2017) – while most of the energy loss is due to the pitching torque during the stroke reversal (snapshots B and C).

Leading up to snapshot D both cases have similar performances before repeating the same behaviour for the second half of the cycle.

3.6. Effects of increased trailing heave amplitude

The previous results, and all prior published results, have focused on tandem foils that share the same heave amplitude. However, figure 7 demonstrates that increasing the trailing heave amplitude leads to increased system performance. We can identify three reasons for this benefit. Firstly, the higher values of h_{tr} sample higher momentum fluid (figure 5a). Secondly, larger heave amplitudes provide easier LEV avoidance, similar to that discussed in connection to figure 10. Lastly, the larger trailing heave amplitude does provide new mechanisms for constructive wake interactions. For example, figure 9(a) shows a dramatic increase in system performance for an enlarged trailing heave due to a small shift in the wake phase, Φ (cyan and pink triangles). These two cases are discussed in this section, and are illustrated in figure 11.

In both the constructive and destructive cases (figure 11a,b), the trailing foil can reach the outer extent of the instantaneous wake region and take advantage of the accelerated velocity. Note that both cases display direct collisions with wake vortices. By looking closely at the position of the vortex relative to the trailing foil we can observe that both cases initially see reduced dynamic pressure near the foil due to the wake vortex (figure 11a,b, A–B), evident in the lower-magnitude region near the trailing foil's leading edge. However, further in the cycle the constructive case demonstrates a significant increase in dynamic pressure as the trailing foil collides with the vortex, evident by observing the region near the upper surface of the foil at the leading edge (figure 11a, C). This is in contrast with the destructive case that, due to this vortex encounter happening at an earlier time in the cycle, displays decreased dynamic pressure at the same instant (figure 11b, C).

It is also clear that the two cases have approximately equal performance at the points in the cycle with high heave velocity, \dot{h} (figure 11, A,D). This is likely due to flow being dominated by the attached LEV during this phase of the cycle. The differences occur during the stroke reversal part of the oscillation (snapshots B–C). In snapshot B of the constructive case (figure 11a), as the foil reaches its maximum heave amplitude, it begins to shed its attached LEV and loses its lift, C_L (figure 11c, B). After this shedding occurs, the foil collides with the primary LEV in the wake (snapshot C) and gains C_L in alignment

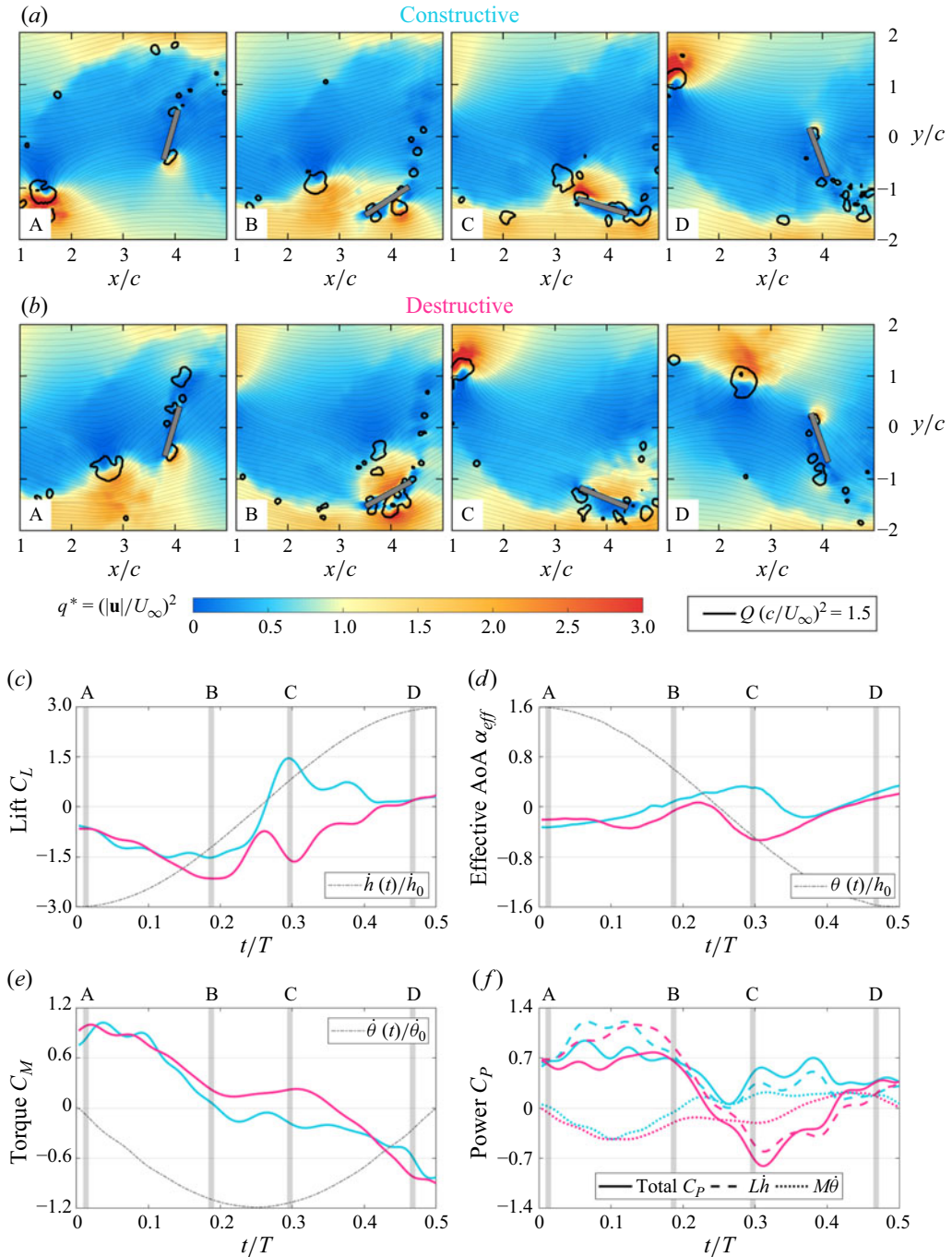


Figure 11. Snapshots of dynamic pressure $q^* = (|\mathbf{u}|/U_\infty)^2$, with instantaneous streamlines of wake-foil interactions for $S_x = 4c$, $\alpha_{T/4,le} = 0.68$, $\theta_{0,tr} = 75^\circ$ and $h_{0,tr} = 1.4c$. Isolines of $Q(c/U_\infty)^2 = 1.5$ are shown to visualise primary vortices. Cases shown are for two values of inter-foil phase: (a) $\psi_{1-2} = -110^\circ$ for the constructive case and (b) $\psi_{1-2} = 180^\circ$ for the destructive case. Also shown are non-dimensional (c) lift, (d) torque, (e) effective angle of attack and (f) power over half of an oscillation cycle. Also shown in (f) are the power contributions from lift and torque.

with its heaving direction, generating positive power, C_P (figure 11c,f, C). During the same part of the cycle, the destructive case sees the trailing foil go around the primary wake LEV and seemingly delay the shedding of its own attached LEV (figure 11b, B). Crucially, snapshot C in figure 11(b) shows that the foil develops a second LEV, absent in the constructive case (although it can also be seen in the earlier configurations discussed in figure 10a,b). The effect of this secondary LEV is reflected in the lift (figure 11c, C), which becomes more negative, and can be correlated to the increase of dynamic pressure near the trailing foil's leading edge. This increase in C_L results in negative C_P being generated because the foil is heaving in the opposite direction at this time (figure 11f, C).

The C_M performance is also affected by the presence or absence of the secondary LEV. Figure 11(e) shows how, while the destructive case experiences positive C_M during the stroke reversal (snapshots B and C), the constructive case C_M becomes slightly negative. The effect is amplified by the high angular velocity at this time.

The result of the small difference in inter-foil phase ψ_{1-2} (and consequently wake phase Φ) is that in the constructive case the foil experiences positive power throughout the cycle. Although this shows how the trailing foil can benefit greatly from vortex–foil interactions, the slight difference in ψ_{1-2} between the constructive and destructive cases demonstrates how the trailing foil's performance is highly sensitive to small changes in kinematics when pursuing strong vortex–foil interactions. This echoes the result from Ma *et al.* (2019) who, in their semi-passive tandem foil system, noted that although favourable wake–foil interactions can yield significantly improved performance, it is more desirable to avoid negative wake–foil interactions than to pursue favourable ones.

These cases exhibit complex vortex dynamics, such as vortex annihilation and enhancement, impacting foil performance. For instance, in the constructive case, the trailing foil's secondary LEV is suppressed by its interaction with the wake LEV. As discussed earlier (figures 10a,b and 11b), a secondary LEV forms on the trailing foil during the stroke reversal. In the constructive case, the collision with the primary wake LEV causes the flow to reorient around the trailing foil's leading edge, keeping the flow attached to its lower side (supported by a positive α_{eff} value at instance C in figure 11d). This also explains the formation of the small LEV on the foil's upper side at this time. In the destructive case, the wake–LEV collision likely enhances the secondary LEV. However, due to the messiness of the wake resulting from these collisions it is not clear what occurs during this interaction, or if there is an additional collision of the trailing foil with the secondary wake LEV (present in figure 11a but not in figure 11b during snapshots C and D). Additionally, vortex dynamics affecting torque performance (figure 11e) is not as obvious. A detailed analysis separating vortex-induced forces from other flow contributions would provide more insight. Previous studies focused primarily on vortex dynamics (Menon & Mittal 2021; Gao *et al.* 2023; Zhu *et al.* 2023) utilised the force and moment partitioning method (Quartapelle & Napolitano 1983) to analyse vortex-induced forces on aerofoils. While this analysis could provide valuable insight into the vortex–foil interactions presented in this work, this is outside the scope of this study and warrants future exploration.

These results also offer insight into different array configurations. While tandem foil configurations can improve performance in an optimal setting, downstream foils are always affected by the decrease in flow momentum due to the leading foil. Several studies (Nishino & Willden 2012; Draper & Nishino 2014; Gebreslassie, Tabor & Belmont 2015; Nuernberg & Tao 2018; Chen, Lin & Liang 2023) have investigated alternative array configurations like tidal fences and staggered arrays. Based on linear actuator disk theory, Draper & Nishino (2014) studied the performances of staggered and centred (tandem) configurations, and showed that in a staggered array downstream turbines take advantage

of the accelerated bypass flow from the leading turbine's wake (recall from [figure 5](#)) to increase their power output. Draper & Nishino (2014) also found that performance in staggered arrays improves when the leading turbine operates with higher flow resistance due to this increased bypass flow available for downstream turbines. This can be applied to oscillating foils in a mean sense, where a trailing foil positioned off-centre could use the accelerated flow during its up- and downstrokes to reach higher peak power. However, it is unclear what the performance losses would look like during the stroke reversal due to these mechanisms, as it is the part in the cycle where the most power is lost. A staggered configuration could also lead to higher power variability within the cycle and more complex vortex–foil interactions. Wake topology becomes critical in multi-turbine configurations, especially with close spacings as those explored in this study. While symmetric shedding patterns occur behind the leading foil, downstream turbine interference creates more complex wake patterns like those observed in studies on oscillating foils within propulsive regimes (Verma & Hemmati 2021; Wei *et al.* 2023). Therefore, if vortex–foil interactions can be minimised (as in the constructive case of [figure 10a](#)), a staggered array could allow the leading foil to operate in a higher $\alpha_{T/4}$ regime to improve its performance and increase the bypass flow's magnitude, which can be harnessed by downstream foils.

4. Conclusions

The optimal kinematics and the role of wake–foil interactions in a tandem hydrofoil array's performance for energy harvesting were studied experimentally. Distinct from previous such studies, we have chosen three operating regimes for the leading foil – the shear-layer, LEV and LEV + TEV regimes. For each of these regimes, we allow the trailing foil to have different kinematics (heave, pitch and phase) from the leading foil. Special attention was paid to the effect that the wake structure prescribed by the leading foil has on the trailing foil. The role of the wake vortices produced by the leading foil in the trailing-foil performance was also analysed in detail.

The strongest effects from wake–foil interactions were observed in the LEV + TEV regime due to the primary vortices being stronger than the main LEV in the intermediate $\alpha_{T/4}$ regime. Modifying the kinematics of the trailing foil, notably increasing the heaving amplitude, led to constructive wake–foil interactions previously not observed in the literature. In this regime, the performance of the trailing foil is highly sensitive to the phase, ψ_{1-2} , between the leading and trailing foils, and we find that dramatically improved or reduced performance can result due to constructive or destructive wake vortex–foil interactions.

The highest system performance observed in the parameter space explored was when the leading foil operated within the LEV regime, different from the single-foil optimum, which is in the LEV + TEV regime. In the LEV regime, the trailing foil does not see its performance affected as dramatically by wake–foil interactions, and the wake deficit encountered is not as strong as in the LEV + TEV regime. This results in the interesting conclusion that for the tandem array to perform optimally, neither foil should operate at its single-foil optimal kinematics. It was also found that although the primary vortices in the LEV and LEV + TEV regimes initially follow different paths after being shed by the leading foil, their trajectories converge as they travel downstream. This results in the primary vortex approaching the trailing foil with the same y location across wake regimes. As observed by previous literature the inter-foil phase directly affects the timing of wake–foil interactions, but we additionally find that the heaving amplitude of the trailing foil

has a significant impact on the type of interactions that occurred, and consequently the harvesting performance.

As has been previously noted, and is studied in some detail here, when the leading and trailing heave amplitudes are matched, constructive interactions are observed for cases that avoid wake structures, while destructive interactions occur when the trailing foil collides with the leading-foil LEV. However, a second kind of constructive interaction is also identified when the trailing foil has heave amplitude larger than that of the leading foil. In this case, the LEV does interact with the trailing foil, but acts to enhance its energy extraction.

This study provides experimental results that support the available literature on OFTs, and expands it by evaluating the performance of a tandem array where both foils have very different kinematics. By highlighting configurations that lead to dramatic performance improvements through wake–foil interactions, these findings illustrate the complex flow features found in interactions that lead to improved energy-harvesting performance. Models that predict array performance, such as that proposed by Ribeiro & Franck (2024), can be enhanced through these findings, especially within the highly unsteady wake regimes highlighted in this study. These results also reinforce the appeal of oscillating flow turbines. While the power coefficient of the individual turbines is lower than, for example, a single horizontal axes turbine, due to the ability to locate tandem turbines in close proximity, the system power density is far higher than that of a conventional turbine array. This operational advantage, combined with other features of OFTs, such as their insensitivity to specific blade design (Kim *et al.* 2017), may lead to greater adoption in renewable energy-harvesting applications.

Acknowledgements. The authors are most grateful to J. Franck and B. Ribeiro for many fruitful discussions.

Funding. This work was supported by the National Science Foundation, Grant 1921359 and AFOSR Grant FA9550-23-1-0478. Y.Z. was supported by AFOSR Grant FA9550-21-1-0462.

Declaration of interests. The authors report no conflict of interest.

REFERENCES

- ASHRAF, M.A., YOUNG, J., LAI, J.C. & PLATZER, M.F. 2011 Numerical analysis of an oscillating-wing wind and hydropower generator. *AIAA J.* **49** (7), 1374–1386.
- CHEN, Y., LIN, B. & LIANG, D. 2023 Interactions between approaching flow and hydrokinetic turbines in a staggered layout. *Renew. Energy* **218**, 119339.
- DABIRI, J.O. 2011 Potential order-of-magnitude enhancement of wind farm power density via counter-rotating vertical-axis wind turbine arrays. *J. Renew. Sustainable Energy* **3** (4), 043104.
- DRAPER, S. & NISHINO, T. 2014 Centred and staggered arrangements of tidal turbines. *J. Fluid Mech.* **739**, 72–93.
- GAO, A.K., CANTWELL, C.D., SON, O. & SHERWIN, S.J. 2023 Three-dimensional transition and force characteristics of low-Reynolds-number flows past a plunging airfoil. *J. Fluid Mech.* **973**, A43.
- GEBRESLASSIE, M.G., TABOR, G.R. & BELMONT, M.R. 2015 Investigation of the performance of a staggered configuration of tidal turbines using cfd. *Renew. Energy* **80**, 690–698.
- GUNGOR, A., KHALID, M.S.U. & HEMMATI, A. 2024 Physics-informed scaling laws for the performance of pitching foils in schooling configurations. *J. R. Soc. Interface* **21** (216), 20240157.
- HE, G., MO, W., GAO, Y., WANG, J., ZHANG, Z., YANG, H. & MAO, W. 2022a Numerical study of a semi-passive oscillating hydrofoil on power-extraction with wing-in-ground effect. *J. Fluid. Struct.* **115**, 103761.
- HE, G., YANG, H., MO, W., ZHAO, Z., WANG, W. & GHASSEMI, H. 2022b Influence of inter-foil spacing on energy extraction of tandem oscillating hydrofoils. *Ocean Engng* **259**, 111953.
- HOULSBY, G., DRAPER, S. & OLDFIELD, M. 2008 Application of linear momentum actuator disc theory to open channel flow.
- HOWLAND, M.F., LELE, S.K. & DABIRI, J.O. 2019 Wind farm power optimization through wake steering. *Proc. Natl Acad. Sci. USA* **116**, 14495–14500.

- JONES, K.D., LINDSEY, K. & PLATZER, M.F. 2003 An investigation of the fluid-structure interaction in an oscillating-wing micro-hydropower generator. *Fluid Struct. Interaction* **71**, 73–82.
- JONES, K.D. & PLATZER, M.F. 1997 Numerical computation of flapping-wing propulsion and power extraction. *AIAA Paper No. 97-0826, 35th AIAA Aerospace Sciences Meeting*, Reno, Nevada.
- KARAKAS, F. & FENERCIOGLU, I. 2016 Effect of side-walls on flapping-wing power-generation: an experimental study. *J. Appl. Fluid Mech.* **9** (6), 2769–2779.
- KARAKAS, F. & FENERCIOGLU, I. 2017 Effect of phase angle on tandem flapping-wing power generation. *Intl J. Energy Prod. Manage.* **2** (1), 95–105.
- KHARE, V. & BHUIYAN, M.A. 2022 Tidal energy-path towards sustainable energy: a technical review.
- KIM, D., STROM, B., MANDRE, S. & BREUER, K. 2017 Energy harvesting performance and flow structure of an oscillating hydrofoil with finite span. *J. Fluid. Struct.* **70**, 314–326.
- KINSEY, T. & DUMAS, G. 2008 Parametric study of an oscillating airfoil in a power-extraction regime. *AIAA J.* **46** (6), 1318–1330.
- KINSEY, T. & DUMAS, G. 2012 Optimal tandem configuration for oscillating-foils hydrokinetic turbine. *J. Fluids Engng* **134** (3), 031103.
- KUANG, L., KATSUCHI, H., ZHOU, D., CHEN, Y., HAN, Z., ZHANG, K., WANG, J., BAO, Y., CAO, Y. & LIU, Y. 2023 Strategy for mitigating wake interference between offshore vertical-axis wind turbines: evaluation of vertically staggered arrangement. *Appl. Energy* **351**, 121850.
- LEE, H., SIMONE, N., SU, Y., ZHU, Y., RIBEIRO, B.L.R., FRANCK, J.A. & BREUER, K. 2022 Leading edge vortex formation and wake trajectory: synthesizing measurements, analysis, and machine learning. *Phys. Rev. Fluids* **7** (7), 074704.
- LI, L., NAGY, M., GRAVING, J.M., BAK-COLEMAN, J., XIE, G. & COUZIN, I.D. 2020 Vortex phase matching as a strategy for schooling in robots and in fish. *Nat. Commun.* **11** (1), 5408.
- MA, P., WANG, Y., XIE, Y., HAN, J., SUN, G. & ZHANG, J. 2019 Effect of wake interaction on the response of two tandem oscillating hydrofoils. *Energy Sci. Engng* **7** (2), 431–442.
- MASKELL, E. 1965 A theory of the blockage effects on bluff bodies and stalled wings in a closed wind tunnel. Tech. Rep. Ministry of Aviation.
- MASSOUH, F. & DOBREV, I. 2007 Exploration of the vortex wake behind of wind turbine rotor. *J. Phys.: Conf. Ser.* **75**, 012036.
- MCKINNEY, W. & DELAURIER, J. 1981 Wingmill: an oscillating-wing windmill. *J. Energy* **5** (2), 109–115.
- MENON, K. & MITTAL, R. 2021 Quantitative analysis of the kinematics and induced aerodynamic loading of individual vortices in vortex-dominated flows: a computation and data-driven approach. *J. Comput. Phys.* **443**, 110515.
- NEWBOLT, J.W., ZHANG, J. & RISTROPH, L. 2019 Flow interactions between uncoordinated flapping swimmers give rise to group cohesion. *Proc. Natl Acad. Sci. USA* **116** (7), 2419–2424.
- NISHINO, T. & WILLDEN, R.H. 2012 The efficiency of an array of tidal turbines partially blocking a wide channel. *J. Fluid Mech.* **708**, 596–606.
- NUERNBERG, M. & TAO, L. 2018 Experimental study of wake characteristics in tidal turbine arrays. *Renew. Energy* **127**, 168–181.
- OSHKAI, P., IVERSON, D., LEE, W. & DUMAS, G. 2022 Reliability study of a fully-passive oscillating foil turbine operating in a periodically-perturbed inflow. *J. Fluid. Struct.* **113**, 103630.
- QUARTAPELLE, L. & NAPOLITANO, M. 1983 Force and moment in incompressible flows. *AIAA J.* **21** (6), 911–913.
- RAMANANARIVO, S., FANG, F., OZA, A., ZHANG, J. & RISTROPH, L. 2016 Flow interactions lead to orderly formations of flapping wings in forward flight. *Phys. Rev. Fluids* **1** (7), 071201.
- RIBEIRO, B.L.R. & FRANCK, J.A. 2023 Machine learning to classify vortex wakes of energy harvesting oscillating foils. *AIAA J.* **61** (3), 1281–1291.
- RIBEIRO, B.L.R. & FRANCK, J.A. 2024 Prediction of energy harvesting efficiency through a wake-foil interaction model for oscillating foil arrays. *J. Fluid Mech.* **996**, A46.
- RIBEIRO, B.L.R., SU, Y., GUILLAUMIN, Q., BREUER, K.S. & FRANCK, J.A. 2021 Wake-foil interactions and energy harvesting efficiency in tandem oscillating foils. *Phys. Rev. Fluids* **6** (7), 074703.
- RIVAL, D., HASS, G. & TROPEA, C. 2011 Recovery of energy from leading- and trailing-edge vortices in tandem-airfoil configurations. *J. Aircraft* **48** (1), 203–211.
- ROSS, H. & POLAGYE, B. 2020 An experimental assessment of analytical blockage corrections for turbines. *Renew. Energy* **152**, 1328–1341.
- SCHERL, I., STROM, B., SHANG, J.K., WILLIAMS, O., POLAGYE, B.L. & BRUNTON, S.L. 2020 Robust principal component analysis for modal decomposition of corrupt fluid flows. *Phys. Rev. Fluids* **5** (5), 054401.

- SIMPSON, B.J. 2009 Experimental studies of flapping foils for energy extraction. Massachusetts Institute of Technology. <https://dspace.mit.edu/handle/1721.1/55283>
- SU, Y. 2019 Energy harvesting and aeroelastic instabilities using prescribed and elastically-mounted pitching and heaving hydrofoils. PhD thesis, Brown University, USA.
- SU, Y. & BREUER, K. 2019 Resonant response and optimal energy harvesting of an elastically mounted pitching and heaving hydrofoil. *Phys. Rev. Fluids* **4** (6), 064701.
- UIHLEIN, A. & MAGAGNA, D. 2016 Wave and tidal current energy - a review of the current state of research beyond technology. *Renew. Sustainable Energy Rev.* **58**, 1070–1081.
- VERMA, S. & HEMMATI, A. 2021 Evolution of wake structures behind oscillating hydrofoils with combined heaving and pitching motion. *J. Fluid Mech.* **927**, A23.
- VERMA, S. & HEMMATI, A. 2024 On the transition in spanwise wake instability characteristics behind oscillating foils. *J. Fluid Mech.* **1000**, A14.
- WANG, G. & NG, B.F. 2023 Energy harvesting performance of a tandem-hydrofoil based closely-interconnected tidal array. *Energy Convers. Manage.* **280**, 116796.
- WEI, C., HU, Q., LI, S. & SHI, X. 2023 Hydrodynamic interactions and wake dynamics of fish schooling in rectangle and diamond formations. *Ocean Engng* **267**, 113258.
- WHITTLESEY, R.W., LISKA, S. & DABIRI, J.O. 2010 Fish schooling as a basis for vertical axis wind turbine farm design*. *Bioinspir. Biomim.* **5** (3), 035005.
- XIAO, Q. & ZHU, Q. 2014 A review on flow energy harvesters based on flapping foils. *J. Fluid. Struct.* **46**, 174–191.
- XU, G. & XU, W. 2017 Energy extraction of two flapping foils with tandem configurations and vortex interactions. *Engng Anal. Bound. Elem.* **82**, 202–209.
- XU, J., SUN, H. & TAN, S. 2016 Wake vortex interaction effects on energy extraction performance of tandem oscillating hydrofoils. *J. Mech. Sci. Technol.* **30** (9), 4227–4237.
- YOUNG, J., LAI, J.C. & PLATZER, M.F. 2014 A review of progress and challenges in flapping foil power generation. *Prog. Aerosp. Sci.* **67**, 2–28.
- ZHAO, F., JIANG, Q., WANG, Z., QADRI, M.N.M., LI, L. & TANG, H. 2023 Interaction of two fully passive flapping foils arranged in tandem and its influence on flow energy harvesting. *Energy* **268**, 126714.
- ZHENG, M. & BAI, Y. 2022 The configuration effect of flapping foils for energy harvesting. *Phys. Fluids* **34** (11), 113608.
- ZHU, Q. 2011 Optimal frequency for flow energy harvesting of a flapping foil. *J. Fluid Mech.* **675**, 495–517.
- ZHU, Y., LEE, H., KUMAR, S., MENON, K., MITTAL, R. & BREUER, K. 2023 Force moment partitioning and scaling analysis of vortices shed by a 2D pitching wing in quiescent fluid. *Exp. Fluids* **64** (10), 158.